International Journal of Hydrogen Energy 159 (2025) 150581

Contents lists available at ScienceDirect

International Journal of Hydrogen Energy

journal homepage: www.elsevier.com/locate/he

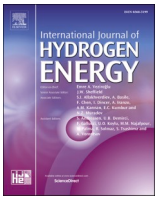

# Composite based on nickel-functionalized carbon nitride and carbon nanotubes as an efficient electrocatalyst for the oxygen evolution reaction

Nicolò Rossetti [a], Veronica Celorrio [b], Goran Dražić [c], Laura Calvillo [a,*]

[a] Dipartimento di Scienze Chimiche, Università di Padova and INSTM Research Unit, Via Marzolo 1, 35131, Padova, Italy
[b] Diamond Light Source Ltd, Diamond House, Harwell Science and Innovation Campus, Didcot, Oxfordshire, OX11 0DE, United Kingdom
[c] Department of Materials Chemistry, National Institute of Chemistry, Hajdrihova 19, SI-1000, Ljubljana, Slovenia

ARTICLE INFO

*Keywords:*
Carbon nanotubes
Carbon nitride
Single atom catalysts
Nickel
Oxygen evolution reaction

ABSTRACT

Single metal atom catalysts (SACs) are receiving widespread attention in electrochemical energy conversion reactions due to the rational use of metal resources and maximum atom utilization efficiency. The role of the support in stabilizing the single atoms is crucial for their catalytic stability. Carbon nitride (CN) is an excellent support for SACs but its low electrical conductivity is not appropriate for electrochemical applications. Here, we report an engineered composite material based on multiwall carbon nanotubes (MWCNTs) and single nickel atoms stabilized on CN (Ni–CN) as efficient and robust electrocatalyst for the oxygen evolution reaction (OER). Composites with different mass Ni–CN:MWCNT ratios have been prepared to optimize the contribution of both materials, and characterized by X-ray diffraction, transmission electron microscopy, X-ray absorption, and X-ray photoemission spectroscopy. Results confirmed the self-assembly of both materials and the condensation of the triazine-based structure of CN into heptazine-based onto the MWCNTs' surface during the synthesis, as well as the presence of single Ni atoms in the composites. The co-presence of NiO nanoparticles was detected for the samples with the highest Ni content. The ratio of NiO nanoparticles to single-atom Ni centers was governed by the Ni–CN:MWCNT ratio employed during synthesis. Electrochemical characterization showed a synergistic effect between Ni–CN and MWCNTs that boosted the OER activity of the composites respect to the individual components. The 1:2 ratio turned out to be the optimal one for the composite preparation, maximizing the combined effects of the catalytic activity of the Ni centers and the electrical conductivity of MWCNTs. The mass activity obtained by this composite was 30 times higher than that of the Ni–CN starting material, attributable to its superior electrical conductivity and improved accessibility of Ni active sites. This study underscores the potential of composite materials to advance SACs toward large-scale application.

## 1. Introduction

The decline in fossil fuel resources and rising $CO_2$ levels are intensifying the search for sustainable and environmentally friendly energy solutions [1–3]. In this evolving energy landscape, hydrogen production via water electrolysis – when powered by renewable sources and free from $CO_2$ emissions – emerges as a key technology for enabling clean mobility and a decarbonized economy [4]. Among electrolysis methods, alkaline water electrolyzers (AWE) stand out due to their technological maturity and their ability to operate with non-noble metal catalysts in alkaline media, thereby reducing both environmental impact and costs [5]. Accordingly, extensive research focuses on developing sustainable, low-cost, efficient, and durable non-noble metal catalysts for the hydrogen evolution reaction (HER) and oxygen evolution reaction (OER) [6].

Despite the promise of transition metals [7], particularly those in the 3d series such as nickel [8–11], the sluggish kinetics and harsh conditions of the OER pose persistent challenges [12]. Efforts to enhance catalytic performance have included tailoring material morphology and reducing catalyst dimensions from bulk to single atoms, which can drastically improve activity due to quantum confinement and surface effects [13–16]. Single-atom catalysts (SACs) maximize atomic efficiency and typically exhibit exceptional activity and selectivity [17], aligning well with sustainability goals by maximizing material usage.

High-performing electrocatalysts must combine high activity with long-term stability. These depend on carefully engineered active sites

* Corresponding author.
*E-mail address:* laura.calvillolamana@unipd.it (L. Calvillo).

https://doi.org/10.1016/j.ijhydene.2025.150581
Received 7 May 2025; Received in revised form 3 July 2025; Accepted 17 July 2025
Available online 22 July 2025

and on the integration of those sites into robust, conductive, and chemically stable support materials. Since electrochemical water splitting occurs at the interface between the catalyst, water, and electrolyte [18,19], optimizing the electrical conductivity of the support is crucial for efficient electron transfer and overall system performance [20–23]. This multifaceted approach, which balances atomic-scale active site engineering with macroscale electrode design, represents a promising pathway for advancing the efficiency and scalability of electrocatalysts in sustainable energy applications [24].

In our previous work, we demonstrated that triazine-based carbon nitride modified with single Ni atoms (Ni–CN) can serve as an effective OER catalyst [25]. Carbon nitride (CN) offers a metal-stabilizing framework with strong Ni–N coordination. In addition, its origin from abundant, nitrogen-rich precursors makes it an attractive, low cost, sustainable material. However, its poor intrinsic conductivity limits its practical application in electrocatalysis. To address this, we incorporate Ni–CN into a multiwall carbon nanotube (MWCNT) matrix to enhance conductivity and preserve catalytic performance. MWCNTs, derived from carbon-based feedstocks and known for their high conductivity, thermal stability, and large surface area [26–28], provide a sustainable and high-performance support. Their structure not only facilitates electron transport but also promotes dispersion and accessibility of active sites.

The state of the art of OER catalysts based on SACs mainly consists of transition metal atoms stabilized in carbon-nitrogen materials [29], such as carbon nitride [30], N-doped carbon nanotubes [31] or N-doped graphene [32]. However, only one composite material made of SACs stabilized in carbon nitride-carbon nanotubes composite has been reported for this application, to the best of our knowledge [33]. On the contrary, several composites consisting of metal or oxides or chalcogenides nanoparticles supported on CN-MWCNTs can be found in the literature for this or other applications [34,35]. The synergistic effect between CN and graphitic carbon materials (MWCNTs or graphene) has been demonstrated for energy conversion applications [36–39]. For example, Ma et al. developed a highly efficient oxygen evolution catalyst through the self-assembly of graphitic carbon nitride nanosheets and carbon nanotubes with remarkable higher catalytic activity and stronger durability than Ir-based noble-metal catalysts. This work inspired us to prepare an active and robust OER composite catalyst including single metal atoms that could enhance even more the OER performance.

This work presents a novel composite catalyst combining the atomic efficiency of Ni single atoms anchored in CN with the conductivity and structural advantages of MWCNTs. This hybrid material, synthesized via thermal treatment, was tested as an OER electrocatalyst. Electrochemical results reveal that performance is driven by a synergistic effect between the two materials attributable to MWCNTs' conductivity and surface area, the availability and spatial distribution of Ni active sites, and the improved charge transfer. The development of such composite materials aligns with both performance optimization and sustainability targets, offering a promising route toward cost-effective and environmentally responsible OER catalysts for large-scale applications.

## 2. Experimental section

### 2.1. Materials

Solvents and reagents used in this work were all purchased from Sigma-Aldrich. MWCNTs (outer diameter: 6.0–13.0 nm, inner diameter: 2.0–6.0 nm, length: 2.5–20 μm, surface area 216 $m^2/g$), purity >98 %. Melamine, purity 99 %. Nickel(II) chloride hexahydrate, ReagentPlus®. Sulfuric acid puriss. p.a., ACS reagent, reag. ISO, reag. Ph. Eur., 95.0–97.0 %. Nitric acid puriss. p.a., reag. ISO, reag. Ph. Eur., ≥65 %. Hydrochloric acid puriss. p.a., ACS reagent, reag. ISO, reag. Ph. Eur., fuming, ≥37 %.

### 2.2. Synthesis of Ni–CN/MWCNT composites

Ni–CN (0.88 Ni wt.%) reported in our previous work [25] was mixed with MWCNTs (Multi Wall CNTs, Merck) and subjected to a heat treatment at 550 °C. MWCNTs, before being used, were treated with acid to create hydrophilic functional groups on the surface. Thus, 200 mg of MWCNTs, were dispersed in a 3:1 V/V solution of concentrated $H_2SO_4$ and $HNO_3$ in a 250 mL flask. The resulting mixture was sonicated for 30 min and then magnetically stirred at room temperature for 24 h. After repeated washes with Milli-Q water, MWCNTs were stirred at room temperature for 24 h with 25 mL of 5 M $HNO_3$. After neutralization through washes with Milli-Q water, MWCNTs were lyophilized (1 mbar, −45 °C). For the catalyst preparation, the considered Ni–CN:MWCNTs ratio (Scheme 1) was dispersed in 50 mL of Milli-Q water in a 250 mL flask. The mixture was sonicated for 30 min and then stirred at 50 °C overnight. The resulting mixture was sonicated for 4 h and lyophilized (1 mbar, −45 °C). The obtained material was subjected to a heat treatment under inert atmosphere conducted in a tubular furnace with horizontal arrangement (Carbolite). The apparatus consists of a quartz tube with the material contained inside between two alumina boats arranged on top of each other to create a semi-closed environment. Heat treatment was carried out following three temperature stages: (1) 100 °C for 30 min, (2) 400 °C for 2 h, and (3) 550 °C for 4 h. The temperature ramp was 2 °C $min^{-1}$. Before the treatment, oxygen was removed from the system by flushing $N_2$ at 1000 SCCM for 20 min. Then, during the heat treatment the inert atmosphere was ensured through a constant flow of $N_2$ equal to 50 SCCM.

A CN:MWCNT composite without Ni was prepared from CN and MWCNTs by following the same method described above and using a 1:2 mass ratio.

### 2.3. Physicochemical characterization

Transmission electron microscopy (TEM) images were acquired with a FEI Tecnai G12 microscope to investigate the morphology of the composites. To detect the single metal atoms, high resolution scanning transmission electron microscopy (STEM) analyses were performed on a probe Cs-corrected scanning transmission electron microscope, JEOL ARM 200 CF, operated at 80 keV to reduce the impact of the electron beam on the sample. The probe semiconvergence angle was 24 mrad and the high-angle annular dark-field (HAADF) detection angles were set to 68–185 mrad. For chemical analysis a Jeol Centurio energy-dispersive X-ray spectroscopy (EDXS) system with a 100 $mm^2$ SDD detector and Gatan Quantum ER double EELS spectrometer were used. X-ray diffraction (XRD) characterization was performed with a Bruker D8 Advance, operating with Cu $K_\alpha$ radiation ($\lambda = 0.15406$ nm) generated at 40 kV and 40 mA to analyze the different components in the composite and the possible formation of Ni nanoparticles. The determination of the different carbon and nitrogen species was made by X-ray photoelectron spectroscopy (XPS) measurements that were acquired in a custom-made UHV system working at a base pressure of $10^{-10}$ mbar, equipped with an Omicron EA125 electron analyser and an X-ray source with a dual Al–Mg anode. Core-level photoemission spectra (C 1s, N 1s, O 1s) were collected at room temperature with a non-monochromatized Al $K_\alpha$ X-ray source (1486.3 eV). Single spectra were acquired using 0.1 eV steps, 0.5 s collection time, and 20 eV pass energy. To analyze the single components of the C 1s and N 1s regions, the spectra were separated into chemically shifted components. For the C 1s region, an asymmetrical shape was used for the $sp^2$ component, whereas symmetrical Voight functions were used for the $sp^3$ component, the C–O functional groups and C-$(N)_3$ species. For the N 1s region, symmetrical Voight functions were used. The nickel oxidation state as well as its coordination were studied by X-ray adsorption spectroscopy (XAS) measurements. They were recorded on beamline B18 at the Diamond Light Source (UK) with ring energy of 3 GeV and a current of 300 mA. The monochromator used was Si(111) crystals operating in Quick EXAFS (QEXAFS) mode. Pellets

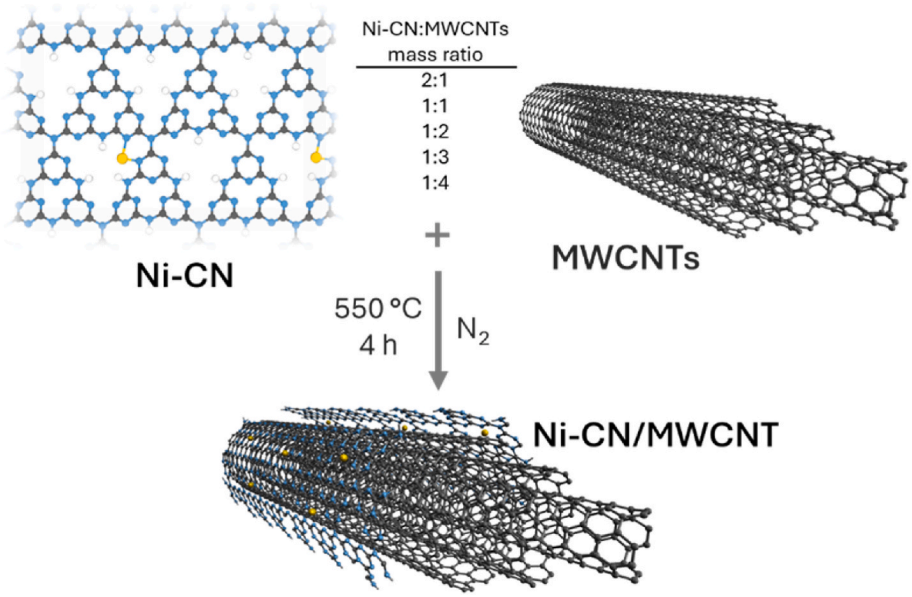


**Scheme 1.** Scheme of the composites synthesis and list of samples prepared.

of Ni–CN/MWCNT and the oxide/hydroxide used as references were measured in fluorescence mode at the Ni K (3333 eV) absorption edge at 298 K using a 36-element Ge detector. The Ni foil was measured simultaneously. Calibration of the monochromator was carried out using the Ni foil previously to the measurements. The acquired data were processed and normalized using Athena.

### 2.4. Electrochemical characterization

Electrochemical measurements were conducted in a custom-made polypropylene three-electrode cell using a mercury oxide electrode (Hg/HgO, 4.24 M KOH, +0.098 V vs RHE) as reference electrode and graphite rod as counter electrode. All the experiments were performed at room temperature. The currents reported are normalized by the electrode geometric area and the potential values are referred to reversible hydrogen electrode (RHE). The working electrode consisted of a thin-film catalyst layer deposited on a glassy carbon (GC) rotating disk electrode (RDE) (3 mm diameter). Before the catalyst modification, the GC electrode was polished with 0.25 μm diamond paste and sonicated in isopropyl alcohol. The catalyst ink was prepared by mixing 1 mg of catalyst, 100 μl of ethanol, 400 μl of Milli-Q water and 5 μl Nafion® (5 wt%, Sigma-Aldrich). The ink was sonicated for 40 min to facilitate the dispersion of the catalyst. An aliquot of 20 μl was deposited by drop casting on the GC (catalyst loading of 0.56 mg $cm^{-2}$). After ink deposition, the electrodes were dried in air. Linear sweep voltammetries (LSVs) at 1600 r.p.m. were acquired at 5 mV $s^{-1}$ in $O_2$-saturated 0.1 M KOH, prepared from high purity reagents (Sigma-Aldrich). All the LSVs reported in this work are IR corrected. The ohmic drop resistance in the solution was determined by electrochemical impedance spectroscopy (68 Ω for the 0.1 M KOH solution). The ohmic drop compensation was performed during the data treatment. The error bars were calculated by performing at least two experiments. RRDE measurements were performed in a three-electrode cell with the same experimental setup detailed above. An aliquot of 14 μl of ink was deposited by drop casting on the GC disk (5 mm diameter) (catalyst loading of 0.143 mg $cm^{-2}$). Polarization curves at 1600 r.p.m. were acquired with a scan rate of 5 mV $s^{-1}$ in $N_2$-saturated 0.1 M KOH, prepared from high purity reagents (Sigma-Aldrich). The best composite (1:2) was subjected to a stress treatment, involving 3000 potential cycles between +1.29 and + 1.64 V vs. RHE at a scan rate of 50 mV $s^{-1}$ in 0.1 M KOH. In addition, a 24 h chronoamperometry (CA) measurement in 0.1 M KOH at 1.61 V vs. RHE was performed on the same composite. In this case, a button electrode was prepared by modifying a carbon paper electrode (1 × 1 cm) with the 1:2 composite (catalyst loading: 0.566 mg $cm^{-2}$). After the CA, the electrode was analyzed by XPS to investigate the material stability. Electrochemical impedance spectroscopy (EIS) measurements were performed at 1.60 V vs. RHE over a frequency range of 100 kHz to 0.1 Hz, using a sinusoidal amplitude of 10 mV. The resulting EIS data were analyzed and fitted to an equivalent circuit model using Nova software.

## 3. Results and discussion

### 3.1. Morphological and structural characterization

A composite material based on multiwall carbon nanotubes (MWCNTs) covered by carbon nitride (CN) modified with single Ni atoms was obtained by a thermal treatment, as described in the Experimental section. The aim was to combine the high electrical conductivity of MWCNTs with the ability of CN to stabilize single atoms. MWCNTs were purchased from Sigma-Aldrich, while Ni–CN was studied as OER catalyst in our previous work [25]. MWCNTs, before being used, were subjected to an acid treatment to create hydrophilic functional groups on the surface. Different mass Ni–CN:MWCNTs ratios were studied to optimize the contribution of both materials in the composite. For simplicity, composites were labelled by using the mass Ni–CN:MWCNTs ratio employed in the synthesis (Scheme 1). The temperature (550 °C) chosen for the thermal treatment was the one that is usually used for the thermal synthesis of graphitic carbon nitride (gCN) from C- and N-containing organic precursors [40–42]. Our aim was to induce the further condensation of CN from the triazine-based structure to the heptazine-based one but not its decomposition [43–47].

Before the thermal treatment, Ni–CN and MWCNTs were dispersed in water to induce the self-assembly of both materials, driven by π–π* stacking interactions between CN and MWCNTs [36,39,48]. In this way, we expect that Ni–CN is dispersed onto the MWCNTs' surface, as depicted in Scheme 1, instead of forming a physical mixture of two materials. TEM images after the thermal treatment confirm that this structure is maintained during the thermal treatment and that CN condensates at the MWCNTs' surface (Fig. S1a–c). In addition, the thermal treatment did not cause any morphological change of the MWCNTs, as shown in Fig. 1a. The homogeneous dispersion of Ni–CN on the MWCNTs' surface is also verified by EDX mapping for C, N, Ni, and O

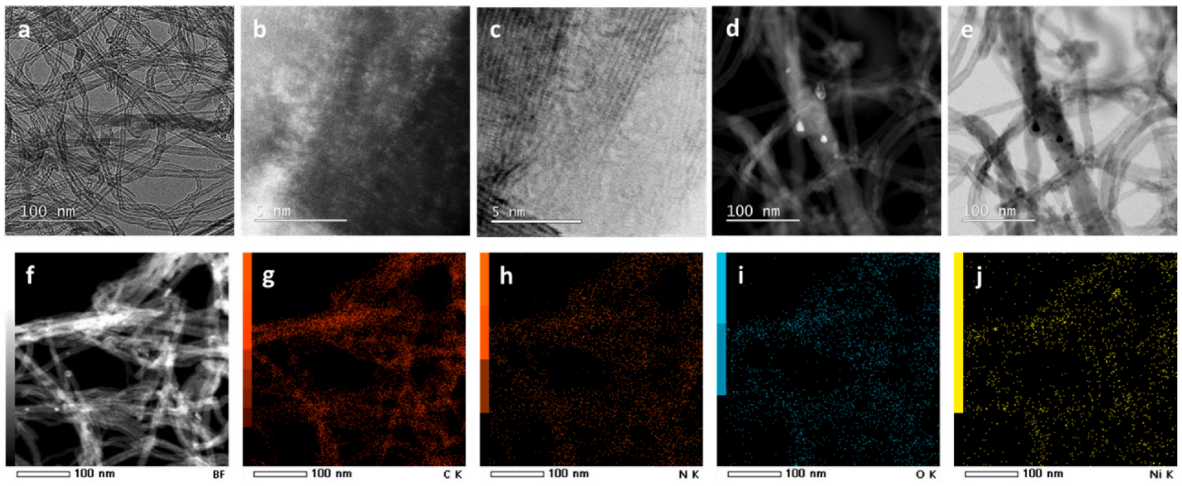


**Fig. 1.** Morphological characterization of the 1:2 sample: (a) representative TEM image, (b,d) HAADF-STEM and (c,e) BF-STEM images, (f) dark field (DF)-STEM image and (g–f) corresponding elemental mapping images of C, N, O, and Ni.

elements shown in Fig. 1f–j. N K and Ni K maps demonstrate that Ni–CN is only present at the surface of the nanotubes since no N or Ni are observed in the regions where the carbon nanotubes are not present, confirming the close interaction between CN and MWCNTs through π–π* stacking interactions. The presence of Ni single atoms was demonstrated by HAADF-STEM and bright field (BF)-STEM images (Fig. 1b and c), where the metal atoms are observed as bright and dark dots, respectively. However, some Ni-based nanoparticles were also formed during

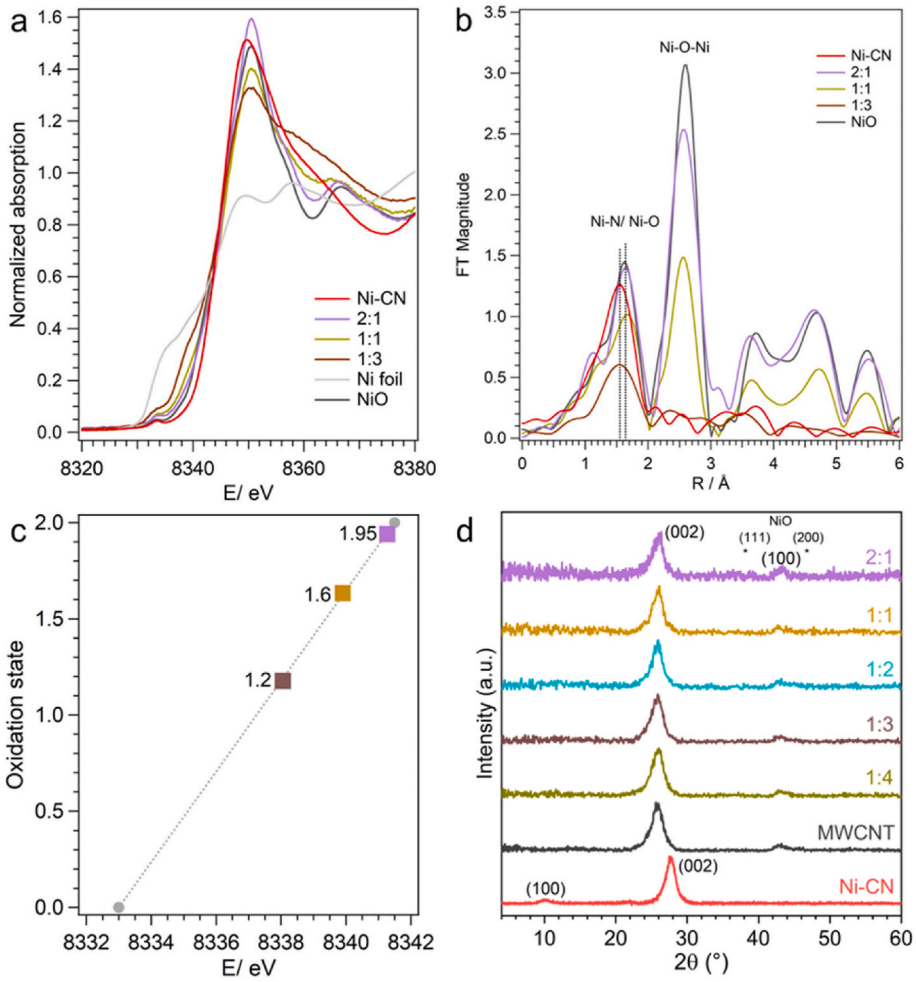


**Fig. 2.** Local structure of Ni centers in Ni–CN/MWCNT. (a) XANES region and (b) uncorrected phase FT EXAFS spectra at the Ni K edge for Ni–CN/MWCNT samples with different Ni–CN:CNT ratio; (c) oxidation state as a function of the absorption edge; and (d) XRD patterns. Ni–CN and MWCNTs patterns are included as references in (d). The XANES and FT EXAFS spectra for the samples used as reference have been included in (a) and (b) for comparison.

the thermal treatment in the samples with the highest Ni content, as seen in Fig. 1d and e and S2. The amount of Ni nanoparticles was directly proportional to the initial amount of Ni. Fig. S2 and S3 report the TEM images for the composite with the highest (2:1) and one with the lowest (1:3) Ni content, respectively. It is observed that Ni is present mainly as Ni-based nanoparticles in the 2:1 composite, ranging from 5 nm to 20 nm, while only Ni single atoms (SAs) are seen in the 1:3 composite (see also XAS characterization below). Particles with two different shapes are observed in the 2:1 composite (Fig. S2 and S4), spherical particles with size from 3 nm to 7 nm, and elongated particles with sizes between 10 nm and 20 nm. The heterogeneous particle size and shape distribution in this composite with high amount of Ni could be attributed to a non-homogeneous dispersion and self-assembly of Ni–CN and MWCNTs due to the excess of Ni–CN. In the 1:2 composite, a small amount of spherical particles ranging from 2 nm to 16 nm are observed in just a few regions (Fig. S5). To quantify the particles density in composites with different amount of Ni, statistical analysis was done, showing that the Ni-based particles coverage is 8.2 % (average from 3 different regions with 11.4 %, 7.5 % and 5.86 %), 0.65 %, and 0 % for the 2:1, 1:2 and 1:3 composites, respectively. Therefore, it can be concluded that the higher the Ni content in the initial Ni–CN:MWCNT mixture, the higher the amount of Ni nanoparticles formed.

The local structure of the Ni centers at the atomic level was investigated via X-ray absorption spectroscopy (XAS). The X-ray absorption near-edge structure (XANES) data and the corresponding Fourier-transform (FT) of the extended X-ray absorption fine structure (EXAFS) spectra are shown in Fig. 2a and b, respectively. The analysis of the XANES region indicates that the oxidation state of Ni was close to +2 for the sample with the highest Ni content (2:1), which could be associated with the formation of Ni nanoparticles (in the form of NiO), as observed by TEM. The Ni oxidation state, however, slightly decreases when the Ni content decreases (Fig. 2c). This result could be related to the lower content of Ni nanoparticles (NPs) and higher content of Ni single atoms (SAs), which either suffer of an electronic effect from MWCNTs or are reduced during the thermal treatment. The analysis of the FT EXAFS spectra indicates that only the sample with the lowest amount of Ni (1:3) contains the metal as only single atoms. This is deduced from the presence of only one peak at 1.5 Å attributed to Ni–N interactions [25,49,50]. For the rest of the samples, a new peak at 2.6 Å, related to Ni–*O*–Ni interactions in NiO [51,52], appears and increases with the Ni loading. In addition, a shift from 1.5 Å to 1.7 Å of the first peak is observed, which is also in agreement with the presence of NiO nanoparticles. Looking at the intensity ratio between the peaks at 1.5–1.7 Å and 2.6 Å, it can be deduced that the formation of NiO nanoparticles is favored by high Ni contents, as expected. This confirms the coexistence of Ni single atoms and NiO nanoparticles in the samples,

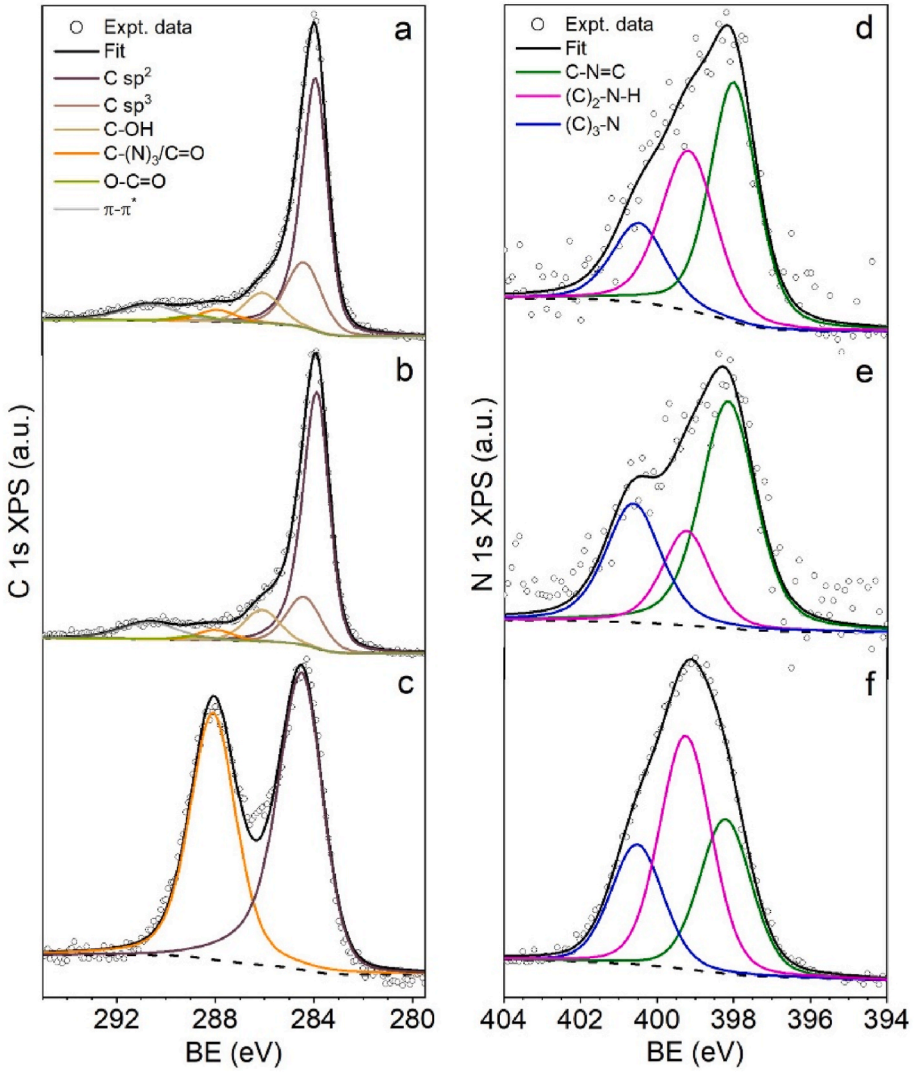


**Fig. 3.** Experimental XPS data: C 1s region of (a) 1:2 sample, (b) acid treated MWCNTs and (c) Ni–CN. N 1s region of (d) 1:2 sample, (e) 1:2 sample without Ni, and (f) Ni–CN.

as observed by high resolution TEM.

The XRD patterns of the hybrid materials (Fig. 2d) only show two diffraction peaks at 25.9° and 43.1° related to the (002) reflection of the hexagonal graphite structure and the (100) graphitic planes of MWCNTs, respectively [53,54]. The absence of secondary peaks related to Ni phases (metal, (hydr)oxides, carbides or nitrides expected in the region between 35° and 60°) [55–57] suggests that the amount of NiO nanoparticles observed by EXAFS is very small to be detected by this technique. The two diffraction peaks related to the (100) and (002) planes of CN, are not observed in the composites probably due to the small amount of this material or its amorphization during the thermal treatment. It should be considered that the position of the (100) and (002) planes slightly changes with the type of CN polymorph [58,59]. In our Ni–CN, they are observed at 10.6° and 27.6°, respectively. However, the expected positions for a heptazine-based structure are 13.1° and 27.3° [59,60]. The most intense peak at around 27.3° overlaps with the (002) plane of MWCNTs.

XPS measurements were conducted to obtain detailed insights into the carbon and nitrogen species present in the materials and confirm the evolution of the CN structure from triazine to heptazine units. Fig. 3a–c presents a comparative analysis of the C 1s region for the 1:2 sample with the MWCNTs and Ni–CN references, while the analysis of all the composites is reported in Table S1. In the 1:2 sample, the most prominent peak at 284.0 eV corresponds to C $sp^2$, characteristic of the MWCNTs graphitic structure [61]. The peak at 284.4 eV is attributed to $sp^3$-type C–C bonds, indicative of defects between conjugated rings in MWCNTs [62]. Additional peaks at 286.1 eV, 287.9 eV, and 288.8 eV are associated with alcoholic (C–OH), carbonyl (C═O), and carboxylic (O–C═O) groups, respectively [62,63]. The acid treatment performed to the as-received MWCNTs enhances the presence of these oxygenated groups with an increase in C–OH species that enhances the hydrophilicity of the carbon nanotubes (Table S1 and S2). No significant differences were observed in the C 1s region between MWCNTs (Fig. 3b) and the 1:2 sample regarding peak positions and C species ratios (Table S1). This indicates that the catalyst dispersion does not alter the carbon structure of the MWCNTs, corroborating observations from TEM and XRD. It should be noted that the C–$(N)_3$ component at 288.1 eV, characteristic of the CN material (Fig. 3c), overlaps with the C═O component at 287.9 eV. However, this component does not increase significantly in the composite materials (Table S1), likely due to the small amount of CN-condensed material. The peak at 291.0 eV, observed in MWCNTs and the 1:2 sample, corresponds to the π–π* transition [64].

Analysis of the N 1s region for the 1:2 sample (Fig. 3d) provides evidence of CN condensation into a heptazine-type structure on the MWCNT surface during the thermal treatment [33,49,65]. Peaks at 398.0, 399.2, and 400.5 eV are associated with pyridinic nitrogen (C–N═C) [66], $(C)_2$–N–H species related to incomplete polymerization of heptazinic units [65], and $(C)_3$–N species [67], respectively. Comparison of the N 1s region of CN [25] and CN:MWCNT (Fig. S6) reveals a decrease in the $(C)_2$–N–H component from 40.0 % to 19.4 % after thermal treatment, which is attributed to the condensation of triazine units into heptazine ones. Notably, the 399.2 eV component, related to $(C)_2$–N–H component, increases in the Ni-modified 1:2 sample, compared with the CN:MWCNT composite (Fig. 3d and e), due to the overlapping with the Ni–N component in this region [25,68], and confirming that Ni single atoms are stabilized through Ni–N interactions. Additionally, the pyridinic component shifts from 398.2 eV (Fig. 3e) to 398.0 eV (Fig. 3d) in the 1:2 sample without and with Ni, respectively, indicating an interaction between Ni and the pyridinic species as expected. This observation is consistent with both theoretical and experimental findings for Ni–CN materials [25]. These results suggest that Ni remains stabilized as single atoms coordinated to pyridinic N, like in Ni–CN. XPS quantification indicates a decrease in Ni content with increasing MWCNTs proportions in the composites, as expected (Table S2).

In summary, TEM, XRD, XAS and XPS measurements validate the synthesis process's efficacy in forming Ni–CN-decorated MWCNTs composite materials. The results confirm the preservation of Ni sites coordinated within a carbon nitride structure that transits from triazine-based to heptazine-based through thermal condensation, and the co-presence of NiO nanoparticles whose amount increases with the Ni loading.

### 3.2. Electrochemical analysis

The Ni–CN:MWCNT composites were evaluated as OER electrocatalysts. Fig. 4a presents the iR corrected LSV curves, which clearly show the significant contribution of MWCNTs to the composites' catalytic activity. All composites exhibit higher catalytic activity than pristine Ni–CN, despite having substantially lower Ni content, as reported in Table S3. This demonstrates that the combination of Ni–CN and MWCNTs leads to synergistic effects, since the overall performance of the composites is better than that of the individual components alone. To further prove that the synergistic effect comes from the intimate interaction established between CN and MWCNTs through self-assembly, a physical mixture of Ni–CN and MWCNTs with a 1:2 mass ratio was prepared and tested (Fig. S7). As expected, the catalytic performance of the physical mixture is intermediate between those for the single components, and much lower than that of the composite with the same composition. This result highlights how the coupling of CN and MWCNTs components can significantly improve the OER catalytic activity.

To elucidate the role of each component, a composite without Ni (CN:MWCNT) was prepared by following the same procedure but using CN instead of Ni–CN (see experimental section). The OER activity of this composite is very similar to that of MWCNTs, although slightly higher, which can be attributed to the presence of nitrogen from CN [36]. The lower current densities displayed by MWCNTs and CN:MWCNTs compared to the Ni–CN:MWCNT composites confirm that nickel is the active catalytic species. This is further supported by the shift in onset potential toward lower values following the incorporation of Ni (Table S3). Regarding the role of CN, it lies in providing nitrogen species able to stabilize the nickel atoms through strong Ni–N interactions. This was further confirmed by performing an acid leaching treatment to remove the NiO nanoparticles that resulted in the degradation of CN through hydrogenation of the $(C)_3$–N bridge sites. The consequence of the CN degradation was the loss of nickel, confirming that Ni was stabilized by CN and not by MWCNTs (see below, Fig. S12). On the other hand, MWCNTs contribute to the electrical conductivity of the composite, improving the charge transfer to/from the Ni catalytic sites. To prove this contribution, electrochemical impedance spectroscopy (EIS) was employed to measure the electron transfer properties in the different materials (Nyquist plots shown in Fig. 4b). Fitting with a Randles-modified equivalent circuit revealed that Ni–CN displays a high charge-transfer resistance ($R_t$) equal to ~36 kΩ, consistent with its poor intrinsic conductivity [69]. Conversely, MWCNTs exhibit a low $R_t$ (~79 Ω) as expected for this type of material and in agreement with values reported in the literature [70,71]. Self-assembly of Ni–CN and MWCNT dramatically reduces $R_t$ in the composite to ~31 Ω, clearly demonstrating that the addition of MWCNTs improves the electron-transport pathways to/from the Ni catalytic sites [48]. Thus, the lowest $R_t$ of the composite confirms intimate electrical coupling between Ni active centers and the MWCNT network, which is critical for efficient electron transfer and enhanced OER performance.

The reaction kinetics was investigated by performing the Tafel analysis. Respect to MWCNTs, a decrease of the Tafel slope (*b*) (Table S3) was observed in the composite materials from 74 to ~54 mV $dec^{-1}$. A Tafel slope of approximately 50 mV $dec^{-1}$ is consistently observed for all Ni-based materials, indicating a similar reaction mechanism across all Ni active sites. This value implies that the rate-determining step is the deprotonation of the M–*OH centers [72], which is consistent with findings reported in the literature for Ni-based

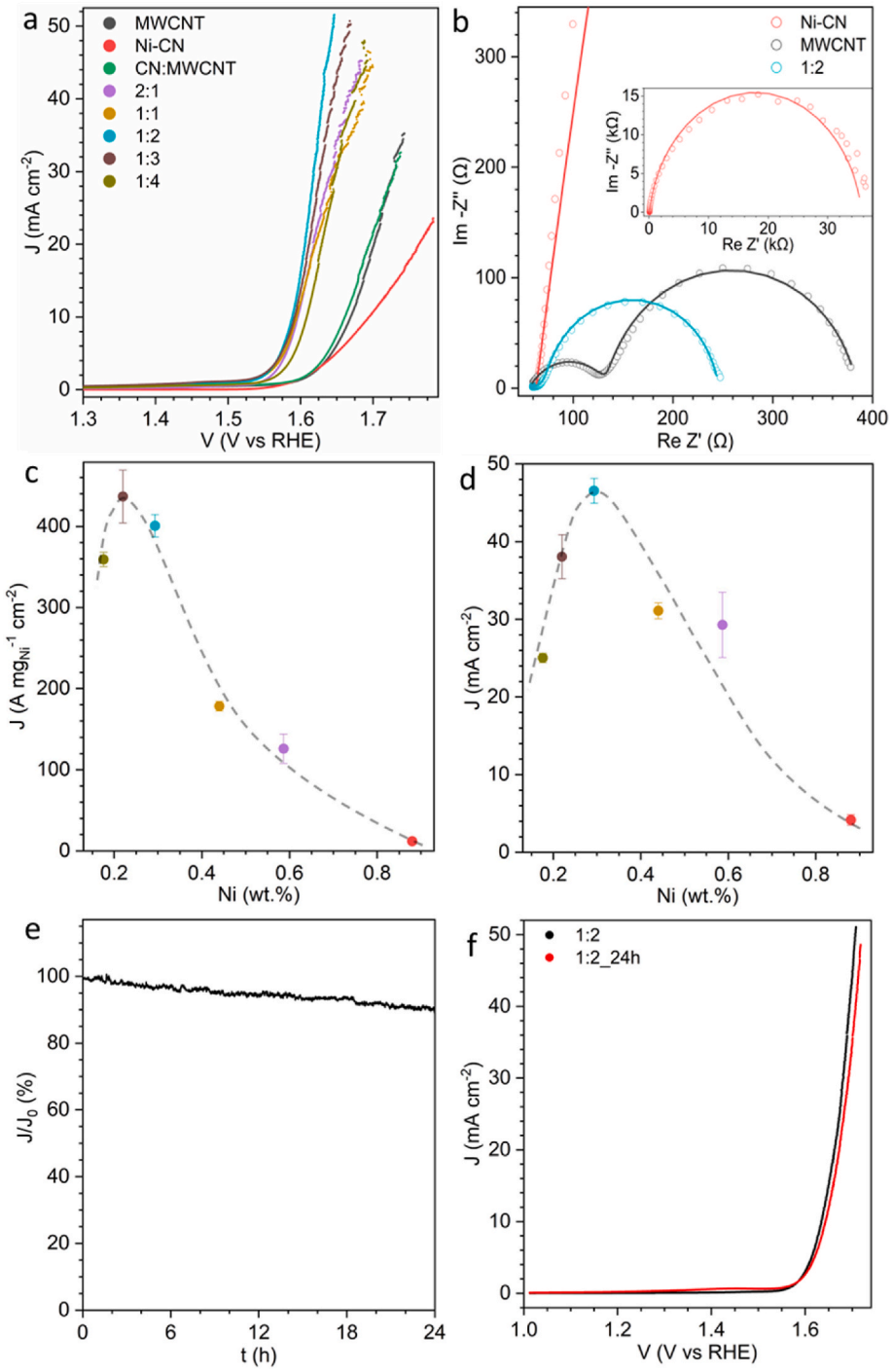


**Fig. 4.** Electrochemical characterization. (a) RDE (1600 r.p.m.) LSVs in $O_2$-saturated 0.1 M KOH (current normalized by geometric area); (b) EIS of Ni–CN, MWCNT, and 1:2 composite; (c) current density (*J*) generated at 1.65 V vs RHE; (d) mass current density generated at 1.65 V vs RHE as a function of the Ni content; (e) CA at 1.61 V vs RHE for 24 h; and (f) LSVs in $O_2$-saturated 0.1 M KOH for the 1:2 composite before and after the 24 h CA. MWCNTs, CN:MWCNT, and Ni–CN are also included as references. All reported values are iR corrected (see description in Section 2.4). Ni content values are referred to Table S3.

carbon matrix catalyst [51,73,74].

To confirm that the generated current is only related to the OER and not to the oxidation of the samples, rotating ring disk electrode (RRDE) measurements were performed (Fig. S8). The current recorded at the Pt disk corresponds to the reduction of the oxygen generated at the catalyst-modified disk. As observed in Fig. S8, the increase of the currents (in absolute value) at both the disk and the ring starts simultaneously, revealing that the observed currents are only related to the OER.

Fig. 4b shows the current density at 1.65 V vs. RHE, obtained from Fig. 4a, for all the samples as a function of the Ni content (referred to Table S3). The selected potential lies within the OER faradaic region, reflecting the catalytic performance of the materials. As can be seen, the highest current is displayed by the 1:2 sample, suggesting that the 1:2 ratio is the optimal one for the composite preparation, maximizing the combined effects of the catalytic activity of the Ni centers and the electrical conductivity of MWCNTs. The current density obtained by this composite (47 mA $cm^{-2}$) is 10 times higher than that of the starting

Ni–CN material (4 mA $cm^{-2}$), even if it only contains 0.29 wt% Ni (3 times less Ni than in Ni–CN). It must be highlighted that the direct comparison between Ni–CN and Ni–CN:MWCNT composites is complicated since the Ni content is significantly different. To address this issue, it is critical to evaluate the current density in terms of specific activity per mass of active species, specifically the mass of Ni. Fig. 4c illustrates the current density at 1.65 V vs. RHE normalized by the nominal Ni mass. The trend is very similar to that depicted in Fig. 4b. All composites exhibit higher mass current densities compared to pristine Ni–CN, underscoring the synergistic effect between Ni–CN and MWCNTs in enhancing the catalytic performance. Interestingly, two different regions of mass activity are observed. The first one includes the 2:1 and 1:1 composites, which exhibit specific current densities of 126 and 178 A $mg^{-1}$ $cm^{-2}$, respectively. The second region comprises the 1:2, 1:3, and 1:4 samples, which demonstrate significantly higher specific current densities of 401, 437, and 359 A $mg^{-1}$ $cm^{-2}$, respectively, approximately 30 times greater than that of pristine Ni–CN (12 A $mg^{-1}$ $cm^{-2}$). This result confirms that Ni single atoms have higher specific activity than nanoparticles since, as determined by TEM and XAS, the 2:1 and 1:1 composites contain more Ni nanoparticles than single atoms, whereas the 1:3 sample contains only Ni single atoms. It should be highlighted that Ni utilization in a nanoparticle-based material is smaller than in a single atom-based one and this could lead to an underestimation of the specific activity of the 2:1 and 1:1 composites. However, as seen in Fig. S9, the number of Ni actives sites in these two samples is higher than in the SA-based composites, as deduced from the area of the Ni redox couple. This underscores the pivotal role of SACs in achieving exceptional catalytic performance, as their specific activity far surpasses that of nanoparticle-based catalysts, establishing SACs as the defining factor for the remarkable enhancement observed in the composite materials.

A reference sample was prepared via a one-step thermal synthesis, following the same procedure but simultaneously mixing melamine, MWCNTs, and the Ni precursor. The synthesis is detailed in the ESI. The objective was to determine if the two-step synthesis was worthy to control the composite structure or not. HAADF-STEM and BF-STEM analyses of the one-step sample revealed the presence of Ni single atoms, along with a predominant component of Ni nanoparticles (Fig. S10). The electrochemical tests showed a lower catalytic activity compared to the 1:2 sample (Fig. S11), confirming the effectiveness of the two-step synthesis strategy, in which Ni–CN is first synthesized and subsequently assembled with MWCNTs to form the composite material. It should be noted that Ni content in the one-pot composite material is higher than in the 1:2 one, highlighting the importance of the nature of the Ni sites (nanoparticles vs SACs).

In summary, the electrochemical results, coupled with the analysis of the relationship between catalytic activity and the presence of active sites as nanoparticles or single atoms, demonstrate that the catalytic performance of MWCNT-based composite materials depends on a synergistic balance among the highly conductive and high-surface-area MWCNTs, the quantity of catalytic active sites, and their nature as single atoms or nanoparticles. These results highlight the strategy of supporting SACs on a more conductive, high-surface-area MWCNT matrix as a highly effective approach to obtain a more robust electrocatalyst and improve the OER activity.

To the best of our knowledge, literature contains only one study about Ni single atom electrocatalyst supported on a CN and MWCNT matrix. Liu et al. [33] reported a current density ($J$) of 18 mA $cm^{-2}$ at 1.65 V vs. RHE in 1 M KOH for this material, which is lower than the performance observed for the 1:2 sample, despite being measured in a 1 M KOH electrolyte, a solution with higher electrical conductivity compared to the 0.1 M KOH used in this work. Moreover, their electrocatalyst exhibited poorer reaction kinetics, as indicated by a Tafel slope ($b$) of 184 mV $dec^{-1}$.

Expanding the comparison to Ni SACs on N-doped carbon nanotubes reveals limited studies in the literature. Among them, Liu et al. [75] also developed an OER electrocatalyst encapsulating Ni single atoms in N-doped CNTs. In their approach, acid treatment was employed to remove metallic nanoparticles, although the metal concentration in the material was not specified. The Ni-based catalyst with the highest activity in their study achieved a $J$ of 2 mA $cm^{-2}$ at 1.65 V vs. RHE in 0.1 M KOH, with a Tafel slope of 138 mV $dec^{-1}$. Even in this case, the performance remains lower than that achieved with the 1:2 composite. Similarly, in our study, the 1:2 sample was subjected to an acid treatment with the aim of removing the NiO nanoparticles and seeing if the catalytic activity increased. However, electrochemical analysis revealed a significant decrease in catalytic activity (Fig. S12), even lower than MWCNTs, suggesting the total loss of Ni active sites. This decline is attributed to the degradation of the CN substrate that stabilizes the Ni sites through the hydrogenation of $(C)_2$–N–H and $(C)_3$–N species in the acidic solution [65], leading to the loss of the Ni-coordinating CN sites and, therefore, the loss of Ni single atoms a well as NiO nanoparticles. This result confirms that CN is the one that stabilizes Ni atoms through Ni–N interactions as explained above.

The best performing composite, 1:2, was subjected to a durability test to study its catalytic stability. This study was performed in two different ways to compare the results with the literature. First, the composite was subjected to a cycling treatment and the catalytic activity was evaluated by LSV. As shown in Fig. S14, the LSV curves, before and after the stress, almost overlap, suggesting a good catalytic stability. Analysis of the current density at 1.60 V vs. RHE reveals an activity retention of 84.9 %, which is consistent with the values reported by Liu et al. for a similar composite after the same number of cycles [33]. Second, the composite was exposed to a 24 h chronoamperometric measurement. As seen in Fig. 4f, the composite exhibits a 90.1 % current retention after 24 h. Also in this case, the catalytic activity was evaluated by LSV before and after the long-term measurement (Fig. 4e), showing a similar result to that reported in Fig. S14. The stability of our composite surpasses the stability of CN:MWCNTs composites reported in the literature [36]. Ma et al. reported a current retention of 86.7 % after only 10 h, while ours retains 90 % after 24 h.

To investigate the physicochemical stability of the composite, the 1:2 composite was analyzed by XPS after the 24 h CA measurement. Fig. S13 reports the N 1s region of the composite before and after the electrochemical treatment. As observed, the shape, the components, and their ratio does not change after the electrochemical measurement, suggesting that Ni–CN does not degrade on the MWCNTs'surface under catalytic conditions.

## 4. Conclusions

In this work, we have enhanced the OER catalytic performance of Ni-based SACs by integrating Ni–CN into a composite material with MWCNTs. The aim was to combine the high activity and stability of Ni–CN catalysts with the excellent electrical conductivity and high surface area of MWCNTs, and to optimize the composition by exploring various Ni–CN to MWCNTs mass ratios. The Ni–CN catalyst was incorporated onto the MWCNTs' surface through self-assembly as shown by HRTEM, driven by π–π* stacking interactions between CN and MWCNTs, and subsequent, thermal treatment at 550 °C. At this temperature, the transition of CN from triazine-based structure to a heptazine-based one occurs, as confirmed by XPS. During the thermal treatment, the migration of Ni atoms is favored with the consequent formation of NiO clusters/nanoparticles, as shown by HRTEM and XAS. The Ni single atoms to NiO nanoparticles ratio depends on the initial Ni content. Samples with the highest Ni–CN concentrations result in the co-presence of NiO nanoparticles and single Ni atoms, while samples with the lowest Ni–CN concentrations maintained the single-atom Ni coordination.

The optimized composition resulted to be the 1:2 Ni–CN:MWCNT mass ratio. This composite exhibited a remarkable 30-fold increase in OER mass activity respect to Ni–CN. This activity boost is attributed to the combination of Ni–CN and MWCNTs, which leads to synergistic

effects, since the overall performance of the composites is better than that of the individual components alone. Each component has its own role in the composite. Ni is the catalytic phase, CN stabilizes the Ni single atoms, and MWCNTs provide electrical conductivity and increased surface area, overcoming the inherent semiconductive limitations of CN in electrocatalytic applications. These findings demonstrate that composite materials represent an effective strategy for enhancing the catalytic performance and robustness of SACs, thereby advancing their potential for large-scale applications.

## CRediT authorship contribution statement

**Nicolò Rossetti:** Writing – original draft, Methodology, Investigation, Formal analysis. **Veronica Celorrio:** Writing – review & editing, Formal analysis. **Goran Dražić:** Writing – review & editing, Formal analysis. **Laura Calvillo:** Writing – review & editing, Supervision, Project administration, Funding acquisition, Formal analysis, Conceptualization.

## Declaration of competing interest

The authors declare that they have no known competing financial interests or personal relationships that could have appeared to influence the work reported in this paper.

## Acknowledgements

Authors would like to acknowledge support from the National Recovery and Resilience Plan (NRRP), by the Italian Ministry of University and Research (MUR), funded by the European Union – NextGenerationEU (CYCLE-E, P2022FALAP). L.C. acknowledges funding from Junta de Andalucía - Consejería de Universidad, Investigación e Innovación - Project (P21_00208). N.R. thanks support from MIUR and European Social Fund through the program PON 2014–2020, Project no. DOT1319135-5. G.D. acknowledges the financial support from Slovenian Research Agency (P2-0421, J2-3041). Authors would like to thank Diamond Light Source for providing beamtime (NT40853).

## Appendix B. Supplementary data

Supplementary data to this article can be found online at https://doi.org/10.1016/j.ijhydene.2025.150581.

## Data availability

Data will be made available on request.

## References

[1] Le TT, Sharma P, Bora BJ, Tran VD, Truong TH, Le HC, Nguyen PQP. Fueling the future: a comprehensive review of hydrogen energy systems and their challenges. Int J Hydrogen Energy 2024;54:791–816. https://doi.org/10.1016/j.ijhydene.2023.08.044.

[2] Le P-A, Trung VD, Nguyen PL, Bac Phung TV, Natsuki J, Natsuki T. The current status of hydrogen energy: an overview. RSC Adv 2023;13:28262–87. https://doi.org/10.1039/D3RA05158G.

[3] Jiao Y, Zheng Y, Jaroniec M, Qiao SZ. Design of electrocatalysts for oxygen- and hydrogen-involving energy conversion reactions. Chem Soc Rev 2015;44:2060–86. https://doi.org/10.1039/C4CS00470A.

[4] Badgett A, Brauch J, Saha P, Pivovar B. Decarbonization of the electric power sector and implications for low-cost hydrogen production from water electrolysis. Adv Sustain Sys 2023:2300091. https://doi.org/10.1002/adsu.202300091.

[5] Sharshir SW, Joseph A, Elsayad MM, Tareemi AA, Kandeal AW, Elkadeem MR. A review of recent advances in alkaline electrolyzer for green hydrogen production: performance improvement and applications. Int J Hydrogen Energy 2024;49:458–88. https://doi.org/10.1016/j.ijhydene.2023.08.107.

[6] Li J, Jing Z, Bai H, Chen Z, Osman AI, Farghali M, Rooney DW, Yap P-S. Optimizing hydrogen production by alkaline water decomposition with transition metal-based electrocatalysts. Environ Chem Lett 2023;21:2583–617. https://doi.org/10.1007/s10311-023-01616-z.

[7] Guo T, Li L, Wang Z. Recent development and future perspectives of amorphous transition metal-based electrocatalysts for oxygen evolution reaction. Adv Energy Mater 2022;12:2200827. https://doi.org/10.1002/aenm.202200827.

[8] Yu M, Budiyanto E, Tüysüz H. Principles of water electrolysis and recent progress in cobalt-, nickel-, and iron-based oxides for the oxygen evolution reaction. Angew Chem Int Ed 2022;61:e202103824. https://doi.org/10.1002/anie.202103824.

[9] Vij V, Sultan S, Harzandi AM, Meena A, Tiwari JN, Lee W-G, Yoon T, Kim KS. Nickel-based electrocatalysts for energy-related applications: oxygen reduction, oxygen evolution, and hydrogen evolution reactions. ACS Catal 2017;7:7196–225. https://doi.org/10.1021/acscatal.7b01800.

[10] Subbaraman R, Tripkovic D, Chang K-C, Strmcnik D, Paulikas AP, Hirunsit P, Chan M, Greeley J, Stamenkovic V, Markovic NM. Trends in activity for the water electrolyser reactions on 3d M(Ni,Co,Fe,Mn) hydr(oxy)oxide catalysts. Nat Mater 2012;11:550–7. https://doi.org/10.1038/nmat3313.

[11] Chen Y, Rui K, Zhu J, Dou SX, Sun W. Recent progress on nickel-based oxide/(Oxy) Hydroxide electrocatalysts for the oxygen evolution reaction. Chem Eur J 2019;25:703–13. https://doi.org/10.1002/chem.201802068.

[12] Zhong H, Zhang Q, Yu J, Zhang X, Wu C, Ma Y, An H, Wang H, Zhang J, Wang X, Xue J. Fundamental understanding of structural reconstruction behaviors in oxygen evolution reaction electrocatalysts. Adv Energy Mater 2023;13:2301391. https://doi.org/10.1002/aenm.202301391.

[13] Kaiser SK, Chen Z, Faust Akl D, Mitchell S, Pérez-Ramírez J. Single-atom catalysts across the periodic table. Chem Rev 2020;120:11703–809. https://doi.org/10.1021/acs.chemrev.0c00576.

[14] Mistry H, Reske R, Zeng Z, Zhao Z-J, Greeley J, Strasser P, Cuenya BR. Exceptional size-dependent activity enhancement in the electroreduction of $CO_2$ over Au nanoparticles. J Am Chem Soc 2014;136:16473–6. https://doi.org/10.1021/ja508879j.

[15] Yamamoto K, Imaoka T, Chun W-J, Enoki O, Katoh H, Takenaga M, Sonoi A. Size-specific catalytic activity of platinum clusters enhances oxygen reduction reactions. Nat Chem 2009;1:397–402. https://doi.org/10.1038/nchem.288.

[16] Rong W, Zou H, Zang W, Xi S, Wei S, Long B, Hu J, Ji Y, Duan L. Size-dependent activity and selectivity of atomic-level copper nanoclusters during $CO/CO_2$ electroreduction. Angew Chem Int Ed 2021;60:466–72. https://doi.org/10.1002/anie.202011836.

[17] Cheng Y, Yang S, Jiang SP, Wang S. Supported single atoms as new class of catalysts for electrochemical reduction of carbon dioxide. Small Methods 2019;3:1800440. https://doi.org/10.1002/smtd.201800440.

[18] Yang G, Yu S, Li Y, Li K, Ding L, Xie Z, Wang W, Zhang F-Y. Role of electron pathway in dimensionally increasing water splitting reaction sites in liquid electrolytes. Electrochim Acta 2020;362:137113. https://doi.org/10.1016/j.electacta.2020.137113.

[19] Yang G, Wang W, Xie Z, Yu S, Li Y, Ding L, Li K, Zhang F-Y. Favorable morphology and electronic conductivity of functional sublayers for highly efficient water splitting electrodes. J Energy Storage 2021;36:102342. https://doi.org/10.1016/j.est.2021.102342.

[20] Tsyganok A, Monroy-Castillero P, Piekner Y, Yochelis A, Rothschild A. Parallel water photo-oxidation reaction pathways in hematite photoanodes: implications for solar fuel production. Energy Environ Sci 2022;15:2445–59. https://doi.org/10.1039/D1EE03953A.

[21] Avital YY, Dotan H, Klotz D, Grave DA, Tsyganok A, Gupta B, Kolusheva S, Visoly-Fisher I, Rothschild A, Yochelis A. Two-site H2O2 photo-oxidation on haematite photoanodes. Nat Commun 2018;9:4060. https://doi.org/10.1038/s41467-018-06141-0.

[22] Sinha R, Friedrich D, Zafeiropoulos G, Zoethout E, Parente M, Van De Sanden MCM, Bieberle-Hütter A. Charge carrier dynamics and photocatalytic activity of {111} and {100} faceted Ag3PO4 particles. J Chem Phys 2020;152:244710. https://doi.org/10.1063/5.0006865.

[23] Snir N, Caspary Toroker M. Kinetic properties of oxygen evolution reaction catalysis in hematite. Advcd Theory Sims 2023;6:2300182. https://doi.org/10.1002/adts.202300182.

[24] Hui SR, De Luna P. How increasing proton and electron conduction benefits electrocatalytic CO2 reduction. Matter 2021;4:1555–77. https://doi.org/10.1016/j.matt.2021.02.021.

[25] Rossetti N, Ugolotti A, Cometto C, Celorrio V, Dražić G, Di Valentin C, Calvillo L. Insights into the active nickel centers embedded in graphitic carbon nitride for the oxygen evolution reaction. J Mater Chem A 2024;12:6652–62. https://doi.org/10.1039/D3TA07389K.

[26] Su J, Musgrave CB, Song Y, Huang L, Liu Y, Li G, Xin Y, Xiong P, Li MM-J, Wu H, Zhu M, Chen HM, Zhang J, Shen H, Tang BZ, Robert M, Goddard WA, Ye R. Strain enhances the activity of molecular electrocatalysts via carbon nanotube supports. Nat Catal 2023;6:818–28. https://doi.org/10.1038/s41929-023-01005-3.

[27] Tavakkoli M, Flahaut E, Peljo P, Sainio J, Davodi F, Lobiak EV, Mustonen K, Kauppinen EI. Mesoporous single-atom-doped graphene–carbon nanotube hybrid: synthesis and tunable electrocatalytic activity for oxygen evolution and reduction reactions. ACS Catal 2020;10:4647–58. https://doi.org/10.1021/acscatal.0c00352.

[28] Popov V. Carbon nanotubes: properties and application. Mater Sci Eng R Rep 2004;43:61–102. https://doi.org/10.1016/j.mser.2003.10.001.

[29] Hu M, Li S, Zheng S, Liang X, Zheng J, Pan F. Tuning single-atom catalysts of nitrogen-coordinated transition metals for optimizing oxygen evolution and reduction reactions. J Phys Chem C 2020;124:13168–76. https://doi.org/10.1021/acs.jpcc.0c01998.

[30] Peng S, Wu X, Cheng W, Li X, Cheng Z, Long D-B. Single metal atom anchored graphitic carbon nitride monolayers as promising multifunctional electrocatalysts for the oxygen reduction reaction, oxygen evolution reaction, and hydrogen

evolution reaction. Appl Surf Sci 2025;695:162840. https://doi.org/10.1016/j.apsusc.2025.162840.
[31] Dilpazir S, He H, Li Z, Wang M, Lu P, Liu R, Xie Z, Gao D, Zhang G. Cobalt single atoms immobilized N-doped carbon nanotubes for enhanced bifunctional catalysis toward oxygen reduction and oxygen evolution reactions. ACS Appl Energy Mater 2018;1:3283–91. https://doi.org/10.1021/acsaem.8b00490.
[32] Rebarchik M, Bhandari S, Kropp T, Mavrikakis M. Insights into the oxygen evolution reaction on graphene-based single-atom catalysts from first-principles-informed microkinetic modeling. ACS Catal 2023;13:5225–35. https://doi.org/10.1021/acscatal.3c00474.
[33] Liu D, Ding S, Wu C, Gan W, Wang C, Cao D, ur Rehman Z, Sang Y, Chen S, Zheng X, Wang Y, Ge B, Song L. Synergistic effect of an atomically dual-metal doped catalyst for highly efficient oxygen evolution. J Mater Chem A 2018;6:6840–6. https://doi.org/10.1039/C8TA00550H.
[34] Pawar RC, Kang S, Ahn SH, Lee CS. Gold nanoparticle modified graphitic carbon nitride/multi-walled carbon nanotube (g-$C_3N_4$/CNTs/Au) hybrid photocatalysts for effective water splitting and degradation. RSC Adv 2015;5:24281–92. https://doi.org/10.1039/C4RA15560B.
[35] Li M, Zheng X, Xie L, Yu Y, Jiang J. The synergistic effect of carbon nanotubes and graphitic carbon nitride on the enhanced supercapacitor performance of cobalt diselenide-based composites. New J Chem 2021;45:14808–14. https://doi.org/10.1039/D1NJ02533C.
[36] Ma TY, Dai S, Jaroniec M, Qiao SZ. Graphitic carbon nitride nanosheet–carbon nanotube three-dimensional porous composites as high-performance oxygen evolution electrocatalysts. Angew Chem 2014;126:7409–13. https://doi.org/10.1002/ange.201403946.
[37] Divinagracia-Luzadas M, Kaneko K, Hori K, Paraggua JA, Noda S, Ocon J. Synthesis and evaluation of self–supporting graphitic carbon nitride/carbon nanotube (GCN/CNT) ORR/OER electrodes in aqueous and non–aqueous media. Curr Appl Phys 2025;71:14–26. https://doi.org/10.1016/j.cap.2024.12.001.
[38] Gong Y, Wang J, Wei Z, Zhang P, Li H, Wang Y. Combination of carbon nitride and carbon nanotubes: synergistic catalysts for energy conversion. ChemSusChem 2014;7:2303–9. https://doi.org/10.1002/cssc.201402078.
[39] Ong W-J, Tan L-L, Chai S-P, Yong S-T, Mohamed AR. Surface charge modification via protonation of graphitic carbon nitride (g-C3N4) for electrostatic self-assembly construction of 2D/2D reduced graphene oxide (rGO)/g-C3N4 nanostructures toward enhanced photocatalytic reduction of carbon dioxide to methane. Nano Energy 2015;13:757–70. https://doi.org/10.1016/j.nanoen.2015.03.014.
[40] Thomas A, Fischer A, Goettmann F, Antonietti M, Müller J-O, Schlögl R, Carlsson JM. Graphitic carbon nitride materials: variation of structure and morphology and their use as metal-free catalysts. J Mater Chem 2008;18:4893. https://doi.org/10.1039/b800274f.
[41] Wang X, Blechert S, Antonietti M. Polymeric graphitic carbon nitride for heterogeneous photocatalysis. ACS Catal 2012;2:1596–606. https://doi.org/10.1021/cs300240x.
[42] Wang Y, Wang X, Antonietti M. Polymeric graphitic carbon nitride as a heterogeneous organocatalyst: from photochemistry to multipurpose catalysis to sustainable chemistry. Angew Chem Int Ed 2012;51:68–89. https://doi.org/10.1002/anie.201101182.
[43] Holst JR, Gillan EG. From triazines to heptazines: deciphering the local structure of amorphous nitrogen-rich carbon nitride materials. J Am Chem Soc 2008;130:7373–9. https://doi.org/10.1021/ja709992s.
[44] Kessler FK, Schnick W. From heptazines to triazines – on the formation of poly (triazine imide). Z Anorg Allg Chem 2019;645:857–62. https://doi.org/10.1002/zaac.201900043.
[45] Lotsch BV, Schnick W. New light on an old story: formation of melam during thermal condensation of melamine. Chem Eur J 2007;13:4956–68. https://doi.org/10.1002/chem.200601291.
[46] Liu N, Li T, Zhao Z, Liu J, Luo X, Yuan X, Luo K, He J, Yu D, Zhao Y. From triazine to heptazine: origin of graphitic carbon nitride as a photocatalyst. ACS Omega 2020;5:12557–67. https://doi.org/10.1021/acsomega.0c01607.
[47] Jürgens B, Irran E, Senker J, Kroll P, Müller H, Schnick W. Melem (2,5,8-triamino-tri- *s* -triazine), an important intermediate during condensation of melamine rings to graphitic carbon nitride: synthesis, structure determination by X-ray powder diffractometry, solid-state NMR, and theoretical studies. J Am Chem Soc 2003;125:10288–300. https://doi.org/10.1021/ja0357689.
[48] Zhang H, Huang Y, Hu S, Huang Q, Wei C, Zhang W, Yang W, Dong P, Hao A. Self-assembly of graphitic carbon nitride nanosheets–carbon nanotube composite for electrochemical simultaneous determination of catechol and hydroquinone. Electrochim Acta 2015;176:28–35. https://doi.org/10.1016/j.electacta.2015.06.119.
[49] Feng J, Gao H, Zheng L, Chen Z, Zeng S, Jiang C, Dong H, Liu L, Zhang S, Zhang X. A Mn-N3 single-atom catalyst embedded in graphitic carbon nitride for efficient CO2 electroreduction. Nat Commun 2020;11:4341. https://doi.org/10.1038/s41467-020-18143-y.
[50] Kwak M, Bok J, Lee B-H, Kim J, Seo Y, Kim S, Choi H, Ko W, Hooch Antink W, Lee CW, Yim GH, Seung H, Park C, Lee K-S, Kim D-H, Hyeon T, Yoo D. Ni single atoms on carbon nitride for visible-light-promoted full heterogeneous dual catalysis. Chem Sci 2022;13:8536–42. https://doi.org/10.1039/D2SC02174A.
[51] Wan W, Zhao Y, Wei S, Triana CA, Li J, Arcifa A, Allen CS, Cao R, Patzke GR. Mechanistic insight into the active centers of single/dual-atom Ni/Fe-based oxygen electrocatalysts. Nat Commun 2021;12:5589. https://doi.org/10.1038/s41467-021-25811-0.
[52] Guay D, Tourillon G, Dartyge E, Fontaine A, McBreen J, Pandya KI, O'Grady WE. In-situ time-resolved EXAFS study of the structural modifications occurring in nickel oxide electrodes between their fully oxidized and reduced states. J Electroanal Chem Interfacial Electrochem 1991;305:83–95. https://doi.org/10.1016/0022-0728(91)85204-3.
[53] Das R, Hamid S, Ali Md, Ramakrishna S, Yongzhi W. Carbon nanotubes characterization by X-ray powder diffraction – a review. CNANO 2014;11:23–35. https://doi.org/10.2174/1573413710666140818210043.
[54] Belin T, Epron F. Characterization methods of carbon nanotubes: a review. Mater Sci Eng, B 2005;119:105–18. https://doi.org/10.1016/j.mseb.2005.02.046.
[55] Richardson J. X-ray diffraction study of nickel oxide reduction by hydrogen. Appl Catal Gen 2003;246:137–50. https://doi.org/10.1016/S0926-860X(02)00669-5.
[56] Deabate S, Fourgeot F, Henn F. X-ray diffraction and micro-Raman spectroscopy analysis of new nickel hydroxide obtained by electrodialysis. J Power Sources 2000;87:125–36. https://doi.org/10.1016/S0378-7753(99)00437-1.
[57] Vempaire D, Miraglia S, Sulpice A, Ortega L, Hlil EK, Fruchart D, Pelletier J. Structure and magnetic properties of nickel nitride thin film synthesized by plasma-based ion implantation. J Magn Magn Mater 2004:272–6. https://doi.org/10.1016/j.jmmm.2004.01.069. E843–E844.
[58] Chen Z, Vorobyeva E, Mitchell S, Fako E, López N, Collins SM, Leary RK, Midgley PA, Hauert R, Pérez-Ramírez J. Single-atom heterogeneous catalysts based on distinct carbon nitride scaffolds. Natl Sci Rev 2018;5:642–52. https://doi.org/10.1093/nsr/nwy048.
[59] Gao J, Zhou Y, Li Z, Yan S, Wang N, Zou Z. High-yield synthesis of millimetre-long, semiconducting carbon nitride nanotubes with intense photoluminescence emission and reproducible photoconductivity. Nanoscale 2012;4:3687. https://doi.org/10.1039/c2nr30777d.
[60] Tyborski T, Merschjann C, Orthmann S, Yang F, Lux-Steiner M-C, Schedel-Niedrig T. Crystal structure of polymeric carbon nitride and the determination of its process-temperature-induced modifications. J Phys Condens Matter 2013;25:395402. https://doi.org/10.1088/0953-8984/25/39/395402.
[61] Lakshminarayanan PV, Toghiani H, Pittman CU. Nitric acid oxidation of vapor grown carbon nanofibers. Carbon 2004;42:2433–42. https://doi.org/10.1016/j.carbon.2004.04.040.
[62] Biesinger MC. Accessing the robustness of adventitious carbon for charge referencing (correction) purposes in XPS analysis: insights from a multi-user facility data review. Appl Surf Sci 2022;597:153681. https://doi.org/10.1016/j.apsusc.2022.153681.
[63] de Menezes BRC, Ferreira FV, Silva BC, Simonetti EAN, Bastos TM, Cividanes LS, Thim GP. Effects of octadecylamine functionalization of carbon nanotubes on dispersion, polarity, and mechanical properties of CNT/HDPE nanocomposites. J Mater Sci 2018;53:14311–27. https://doi.org/10.1007/s10853-018-2627-3.
[64] Goetz SA, Nguyen DT, Esser-Kahn AP. Surface modification of carbon black nanoparticles enhances photothermal separation and release of CO2. Carbon 2016;105:126–35. https://doi.org/10.1016/j.carbon.2016.03.053.
[65] Cometto C, Ugolotti A, Grazietti E, Moretto A, Bottaro G, Armelao L, Di Valentin C, Calvillo L, Granozzi G. Copper single-atoms embedded in 2D graphitic carbon nitride for the CO2 reduction. Npj 2D Mater Appl 2021;5:63. https://doi.org/10.1038/s41699-021-00243-y.
[66] Akaike K, Aoyama K, Dekubo S, Onishi A, Kanai K. Characterizing electronic structure near the energy gap of graphitic carbon nitride based on rational interpretation of chemical analysis. Chem Mater 2018;30:2341–52. https://doi.org/10.1021/acs.chemmater.7b05316.
[67] Liu J, Zhang Y, Zhang L, Xie F, Vasileff A, Qiao S. Graphitic carbon nitride (g-$C_3N_4$)-Derived N-rich graphene with tuneable interlayer distance as a high-rate anode for sodium-ion batteries. Adv Mater 2019;31:1901261. https://doi.org/10.1002/adma.201901261.
[68] Wang G, Ma Y, Zhang T, Liu Y, Wang B, Zhang R, Zhao Z. Partial sulphidation to regulate coordination structure of single nickel atoms on graphitic carbon nitride for efficient solar $H_2$ evolution. Small 2023;19:2205758. https://doi.org/10.1002/smll.202205758.
[69] Gowri VM, Ajith A, John SA. Systematic study on morphological, electrochemical impedance, and electrocatalytic activity of graphitic carbon nitride modified on a glassy carbon substrate from sequential exfoliation in water. Langmuir 2021;37:10538–46. https://doi.org/10.1021/acs.langmuir.1c01550.
[70] Yang Z, Wu H. The electrochemical impedance measurements of carbon nanotubes. Chem Phys Lett 2001;343:235–40. https://doi.org/10.1016/S0009-2614(01)00710-2.
[71] Broicher C, Zeng F, Pfänder N, Frisch M, Bisswanger T, Radnik J, Stockmann JM, Palkovits S, Beine AK, Palkovits R. Iron and manganese containing multi-walled carbon nanotubes as electrocatalysts for the oxygen evolution reaction - unravelling influences on activity and stability. ChemCatChem 2020;12:5378–84. https://doi.org/10.1002/cctc.202000944.
[72] Shinagawa T, Garcia-Esparza AT, Takanabe K. Insight on Tafel slopes from a microkinetic analysis of aqueous electrocatalysis for energy conversion. Sci Rep 2015;5:13801. https://doi.org/10.1038/srep13801.
[73] Ohn S, Kim SY, Mun SK, Oh J, Sa YJ, Park S, Joo SH, Kwon SJ, Park S. Molecularly dispersed nickel-containing species on the carbon nitride network as electrocatalysts for the oxygen evolution reaction. Carbon 2017;124:180–7. https://doi.org/10.1016/j.carbon.2017.08.039.
[74] Tomboc GM, Kim T, Jung S, Yoon HJ, Lee K. Modulating the local coordination environment of single-atom catalysts for enhanced catalytic performance in hydrogen/oxygen evolution reaction. Small 2022;18:2105680. https://doi.org/10.1002/smll.202105680.
[75] Liu Y, Jiang H, Zhu Y, Yang X, Li C. Transition metals (Fe, Co, and Ni) encapsulated in nitrogen-doped carbon nanotubes as bi-functional catalysts for oxygen electrode reactions. J Mater Chem A 2016;4:1694–701. https://doi.org/10.1039/C5TA10551J.